PHYSICAL REVIEW MATERIALS **4**, 125003 (2020)

Controllable synthesis and electronic structure characterization of multiple phases of iron telluride thin films

Zhimo Zhang,[1] Min Cai,[1] Rui Li,[1] Fanqi Meng,[2] Qinghua Zhang,[2] Lin Gu,[2] Zijin Ye,[1] Gang Xu,[1]
Ying-Shuang Fu,[1,*] and Wenhao Zhang[1,†]

[1]*School of Physics and Wuhan National High Magnetic Field Center, Huazhong University of Science and Technology, Wuhan 430074, China*
[2]*Beijing National Laboratory for Condensed Matter Physics, Institute of Physics, Chinese Academy of Sciences, Beijing 100190, People's Republic of China*

(Received 12 August 2020; accepted 3 December 2020; published 29 December 2020)

We present an investigation on the controlled growth of epitaxial iron telluride films of multiple phases by molecular beam epitaxy. By optimizing the substrate temperature, we fabricate different phases of α-FeTe, β-FeTe, and $FeTe_2$, respectively, whose crystalline morphologies are determined by means of *in situ* scanning tunneling microscopy/spectroscopy and *ex situ* scanning transmission electron microscopy. While both α- and β-FeTe films are metallic, we uncover a $\sim$185- and 65-mV semiconducting band gap for the (100) and (011) facets of $FeTe_2$ film, respectively, with the former one being compatible with the first principles calculations. Moreover, for $FeTe_2$, we observe reduced gaps with enhanced conductance in the vicinity of edge boundaries, which are dependent on the geometries of step orientation and possibly in correlation to the magnetic anisotropy with structural distortion. Our study provides insight into the controllable synthesis of Fe-Te compounds with variation of stoichiometries and surface terminations, which may generalize to other epitaxial Fe chalcogenide films.

DOI: 10.1103/PhysRevMaterials.4.125003

Benefiting from the simplest composition and crystallographic structure among the Fe-based high-temperature superconductors, Fe chalcogenides (FeS, FeSe, and FeTe) are widely studied to elucidate their fascinating properties and underlying physics [1–4]. For the most concerned superconducting FeSe, it shows nematicity with a critical transition temperature of 9 K [5,6], whose superconducting properties can be greatly tuned under electronic doping, chemical or hydrostatic pressure [7–9]. However, the sister compound FeTe, although sharing a structural resemblance to FeSe, exhibits some unexpected properties with stronger electron correlations. On one hand, while FeSe is a bad metal without static magnetic order [1,8], the ground state of FeTe is bicollinear antiferromagnetic in long range, arising from the nesting of spin density wave order at $\sim$70 K [10]. On the other hand, different from the incredible enhancement of superconductivity in single-layer FeSe films [11–13], the electronic properties of FeTe are likely independent on dimensionality, with similar electronic structure between bulk crystal and thin film [14].

Despite the intriguing but different properties, all Fe chalcogenides are extremely sensitive to their chemical compositions. The superconductivity will be completely suppressed by a tiny amount of excess or insufficient Fe in FeSe and FeS [15,16]. On the contrary, the nonsuperconducting FeTe becomes superconducting in the presence of oxygen incorporation [17], even though the role of oxygen, whether substituting Te atom or staying in the interstitial sites, is still under debate [18]. The fluctuation in stoichiometry may be even more prominent for Fe chalcogenide thin films fabricated by molecular beam epitaxy (MBE). Due to the chalcogen-rich growth conditions, the formation of a nominally stoichiometric Fe_1Se_1 or Fe_1Te_1 composition is inevitably difficult to achieve. The nonstoichiometry is usually originated from the Fe vacancies [19] or interstitial chalcogen atoms [20] considering the superfluous chalcogen flux during growth. Besides, the necessary long-time postannealing process may also introduce excess Fe concentration [21,22]. Recent advances in MBE techniques are reported to partially overcome these obstacles by a low-temperature growth under Te-limited condition [23] or depositing additional small amounts of Fe [24].

The variation of nonstoichiometry further shows an appreciable impact on FeTe. The presence of excess Fe, ranging from 0.02 to 0.13, not only modifies the structural parameters, but also becomes electronically active and easily couples to the FeTe layers with a large magnetic moment ($>2.0\,\mu_B$/Fe) [25–29]. This introduces complex magnetostructural phase transitions, which have been intensively investigated by neutron scattering [30], spin-resolved scanning tunneling microscopy [31], and magnetotransport measurements [32]. Recently, Kang *et al.* reported different phases of FeTe crystals with magnetic order at a thickness down to a few nanometers [33]. They attribute the observed two-dimensional (2D) magnetism to a concomitant lattice distortion and the spin-lattice coupling, implying that the magnetic states can be remarkably affected by the variation in structural phases. Nevertheless, there exists much elusive interplay of crystal, electronic structure, and magnetism in

---

[*] yfu@hust.edu.cn
[†] wenhaozhang@hust.edu.cn

FeTe, highly suggesting the notable importance of stoichiometry and structural phases in determining its diverse properties [31,34]. Previous studies of Fe-Te compounds are dispersed with different synthesis conditions for FeTe films [25–32] and $FeTe_2$ nanoplate/nanoparticle/nanorod [35,36], but the effect of nonstoichiometry on the structural and physical properties remains an open issue, especially for the case of Te. It is thus desirable to effectively synthesize and distinguish multiple Fe-Te phases in a controllable way, as well as *in situ* characterizing their distinct properties.

In this study, we report the MBE growth of three structural phases of Fe-Te films controlled by the substrate temperature, i.e., α-FeTe, β-FeTe, and $FeTe_2$, all under a Te-rich condition and with low substrate temperature during growth to avoid the variation of stoichiometries by high-temperature annealing. While the former two phases are metallic with triangular and square morphologies, respectively, the $FeTe_2$ film exhibits two projections of bulk crystal onto (100) and (011) planes. We utilize scanning tunneling microscopy/spectroscopy (STM/STS) and scanning transmission electron microscopy (STEM) to identify the crystalline structures and surface terminations, as well as characterizing their electronic structures at low temperature. Decreased band gap and edge states are found near the step boundaries of $FeTe_2$, indicating possible magnetic anisotropy with local $FeTe_6$ octahedron distortion. Our recipe of temperature-controlled phases of Fe-Te films is not only a timely addition to the extensive library of synthesizing Fe-Te compounds, both in three dimensions and two dimensions, but also a valuable route for understanding the essential role of stoichiometry in high-temperature superconducting single-layer $FeSe/SrTiO_3$ films.

All samples were prepared by the MBE method, with high purity iron (powder, 99.99%; Alfa Aesar) and tellurium sources (powder, 99.9999%; Alfa Aesar) used for co-evaporation from standard K cells. Prior to deposition, the Nb-doped $SrTiO_3(001)$ substrate (0.7 wt %) was thermally heated to ∼1220 K with a selenium flux for half an hour and then flashed to 1320 K for an hour. The high temperature was achieved by direct current heating, monitoring by an infrared pyrometer. During the growth process, the Fe flux was kept the same at 1370 K, giving a growth rate of ∼0.2 monolayer (MLs)/min for α-FeTe, β-FeTe, and $FeTe_2$. To obtain an atomically flat surface with large terraces, we restrict the film thickness to 2–5 MLs. We precisely controlled the K-cell temperature of Te source (from 513 to 543 K), resulting in a Fe/Te flux ratio of ∼1:3 to 1:15 determined by a quartz crystal oscillator. The MBE pressure was better than 2×10^{-9} mbar. After growth, a postannealing treatment at the growth temperature for 10 min was necessary to improve the film quality. STM/STS measurements were conducted on a commercial STM system (Unisoku-1500) at a base temperature of 5 K [37]. A W tip was used to carry out the STM/STS measurements, which has been cleaned on an Ag substrate. The tunneling spectra and conductance mappings were acquired by a standard lock-in technique with a modulation voltage (V_{mod}) at 983 Hz. The $FeTe_2$ film samples were capped with a ∼20 nm Te protective layer for *ex situ* STEM characterization. The STEM measurements were performed on a JEM ARM-200CF operated at 200 keV and equipped with double spherical aberration (Cs) correctors [38]. The annular dark-field (ADF) images were acquired with a collection angle of 90–370 mrad. For the first-principles calculations, we employed the Vienna *ab initio* simulation package (VASP) code. The projector augmented wave (PAW) pseudopotential and the generalized gradient approximation (GGA) functional were chosen to evaluate the exchange-correlation energy [39].

The stoichiometric FeTe ($\delta = 0$) compound can stabilize into two crystalline structures at ambient pressure: a hexagonal phase named α-FeTe (NiAs-type, space group no. 194, $P6_3nmc$) and a tetragonal β-FeTe (PbO-type, space group no. 129, $P4/nmm$), which are schematically illustrated in Figs. 1(a) and 1(b). In α-FeTe, the Te atoms sit in the center of an Fe octahedron. The neighboring octahedrons are connected by Fe-Fe bonds along the c axis, leading to a more 3D structure, whereas the β-FeTe stacks in a van der Waals layered structure, where two asymmetric Te layers sandwich the central Fe layer with each Fe atom at the apex of a pyramid. We obtain these two phases by precisely controlling the substrate temperature at a fixed Te/Fe flux ratio, where the growth temperature is 20–40 K lower for the hexagonal (<550 K) than the tetragonal one (570–590 K). This means α-FeTe is thermodynamically favorable at a relatively lower temperature, directly opposite the chemical vapor deposition (CVD)-based growth approach, where the β-FeTe is more energetically stable at lower temperature on SiO_2/Si substrates [33]. We also note a similar decline of formation temperature (∼40 K) for α-FeSe than β-FeSe on a graphene substrate [40], reflecting the phase tunability of Fe chalcogenides by MBE growth.

The structures of α- and β-FeTe are visualized from their atomic-resolved STM images in Figs. 1(c) and 1(d), respectively. While the α-FeTe has a triangular lattice, the β-FeTe is arranged in a square lattice with Te terminations, but with the same value of in-plane lattice constant (0.38 ± 0.01 nm). Despite the apparent differences in crystalline structure, the electronic properties of α- and β-FeTe are relatively similar. As shown in Fig. 1(e), both dI/dV curves exhibit an overall "V" shape of densities of states (DOS) with the minimum but finite conductance exactly at the Fermi energy. While the similarity of DOS for both α- and β-FeTe is consistent with previous numerical calculations on the band structures [41], the physical origin of such a V-like feature is still mysterious in previous experiments and may be possibly in relation to the stripe structures driven by the magnetic ground states of FeTe [34,42]. A recent study has predicted a much stronger magnetism with a larger magnetic moment for the hexagonal FeTe than the tetragonal form [41], and an in-plane noncollinear antiferromagnetic spin structure has been also experimentally detected in α-FeSe films [43].

By reducing the temperature of the $SrTiO_3$ substrate down to 420–470 K, we obtain two types of atomically flat surfaces shown in Figs. 2 and 3. Considering the Te-rich growth conditions and relative low substrate temperature, excess Te are easier to integrate beyond stoichiometric FeTe. We then assign these observed phases to the pyrite $FeTe_2$ of orthorhombic structure (space group no. 58, $Pnnm$, $a = 0.526\,\mathrm{nm}$, $b = 0.626\,\mathrm{nm}$, $c = 0.390\,\mathrm{nm}$), whose 3D crystalline schematics is sketched in Fig. 2(a). For the (100) surface in Figs. 2(b) and 2(c), the Fe atom locates at the center of a distorted $FeTe_6$

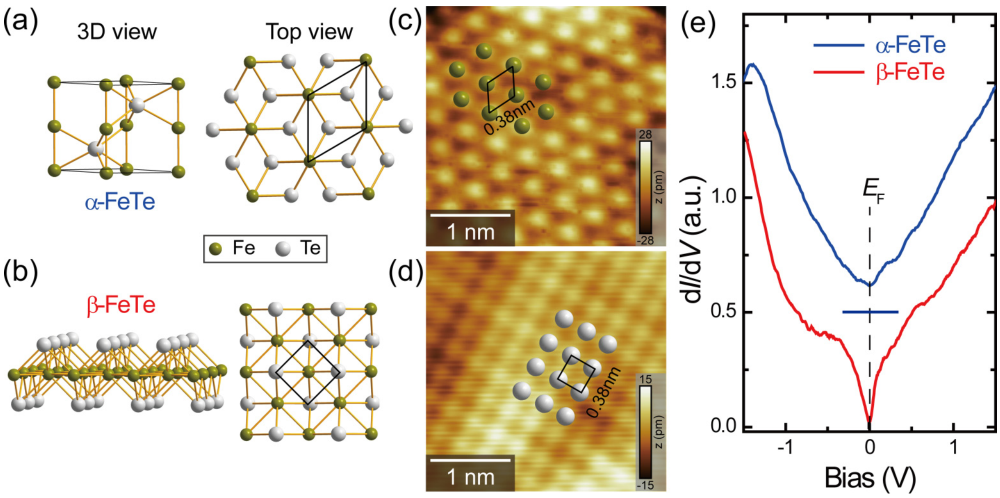

FIG. 1. α- and β-FeTe films grown on a $SrTiO_3$ substrate. (a),(b) 3D and top views of atomic structures for bulk α- and β-FeTe, respectively. (c),(d) High resolution STM images for α- and β-FeTe surface, respectively. Toy models are superposed onto both surfaces, with the unit cell marked as black rhombus and square, respectively. Scanning conditions: $3 \times 3\,\mathrm{nm}^2$, $V_b = +100\,\mathrm{mV}$, $I_t = 50\,\mathrm{pA}$. (e) Comparison of tunneling spectra between α- and β-FeTe films. The y axis is offset for clarity, with the blue horizontal bar marking the zero conductance ($V_b = +0.1\,\mathrm{V}$, $I_t = 100\,\mathrm{pA}$, $V_{\mathrm{mod}} = +1.414\,\mathrm{mV_{rms}}$).

octahedra while Te atoms sit at the apex of it. In the a-b plane, each Fe row is alternately arranged with every two rows of Te, resulting in a 1:2 stoichiometry of $FeTe_2$. Figure 2(d) is a typical STM image of the (100) surface covered with 1D nanorodlike morphology with the island step height of 0.54 ± 0.01 nm [Fig. 2(e)], accompanied by the edges forming an angle of ~60 ° or 120 °. From the atomically resolved STM images in Fig. 2(f), we find the surfaces are pseudohexagonal and constituted with double atomic chains. The unit cell is marked as the black rectangle of (0.38 ± 0.01) nm × (0.63 ± 0.01) nm, well consistent with the b-c facet of $FeTe_2$ (shaped in light blue). Careful inspection indicates that the Te-terminated (100) surface originates from a slightly buckled Te layer with two Te sites: the higher Te-1 connects to two Fe atoms of the underlying Fe layer at a distance of 0.2673 nm, the lower Te-2 singly links to only one Fe atom with the bond length of 0.2560 nm [35,36]. Such corrugation between Fe and Te atoms gives rise to a chainlike STM morphology [Fig. 2(f)] with a lower symmetry, instead of a hexagonal lattice (threefold symmetry).

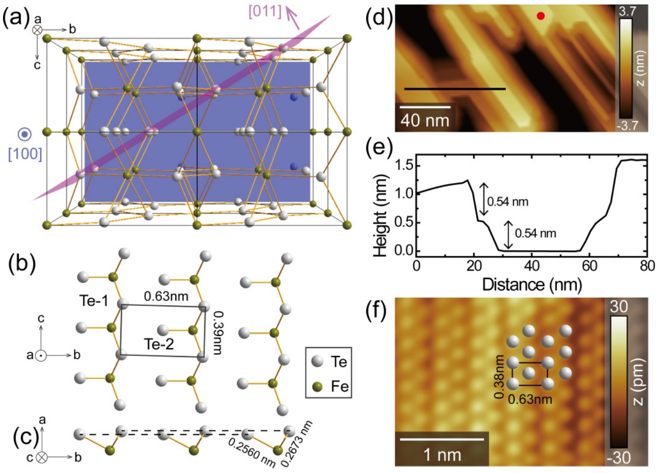

FIG. 2. The (100) surface of orthorhombic $FeTe_2$ films. (a) The crystallographic structure of $FeTe_2$ in a perspective view. Two distinct planes of (100) and (011) are shaded as blue and pink sections, respectively. (b),(c) Top and side views of atomic structure for the (100) plane of $FeTe_2$ lattice, respectively. The topmost Te atoms are slightly buckled. A rectangular unit cell of (0.39 ± 0.01) nm × (0.63 ± 0.01) nm is marked. (d) STM morphology of $FeTe_2$ films oriented along the [100] direction ($200 \times 100\,\mathrm{nm}^2$, $V_b = +2.0\,\mathrm{V}$, $I_t = 10\,\mathrm{pA}$). (e) The line profile across a step edge along the black line in (d), with a step height of 0.54 ± 0.01 nm. (f) The atomically resolved image of the (100) surface. Inset shows a toy model of Te atoms, with the 0.38 nm × 0.63 nm unit cell labeled as black rectangle ($3 \times 2\,\mathrm{nm}^2$, $V_b = +100\,\mathrm{mV}$, $I_t = 50\,\mathrm{pA}$).

There exists another type of STM topographic image in Fig. 3(a) [about 60% compared to the rest 40% of the (100) surface in statistics], with islands adopting irregular shapes with an apparent height of 0.33 ± 0.01 nm. The atomic-resolution STM image in Fig. 3(c) shows a (0.69 ± 0.01) nm × (1.04 ± 0.01) nm lattice, apparently larger than the primitive unit cell of $FeTe_2$ in any low-index surfaces. A previous study had also reported the synthesis of $FeTe_2$ materials in a mixture of 1D nanorods and 2D nanosheets by low-temperature solution chemistry method [44], sharing similar characteristics to our epitaxial $FeTe_2$ films of STM morphologies in Figs. 2(d) and 3(a), respectively. Combining the step height and atomic spacings, we ascribe the observed surface in Fig. 3(a) to the projection of $FeTe_2$ phase onto the (011) plane, as highlighted by the light pink plane in Fig. 2(a). For simplicity, we also display its top and side views in Fig. 3(b). While every Te atom is bonded with two Fe atoms of the underlying Fe layer, the bonding direction is divided into two categories, leading to two rows of Te atoms faulted by half a unit cell length with each other along the b axis. The distance along the [011] direction is 0.33 nm, matching the value of step height in Fig. 3(a) quite well. We can even image the bonding direction near the surface Te atoms, as marked by

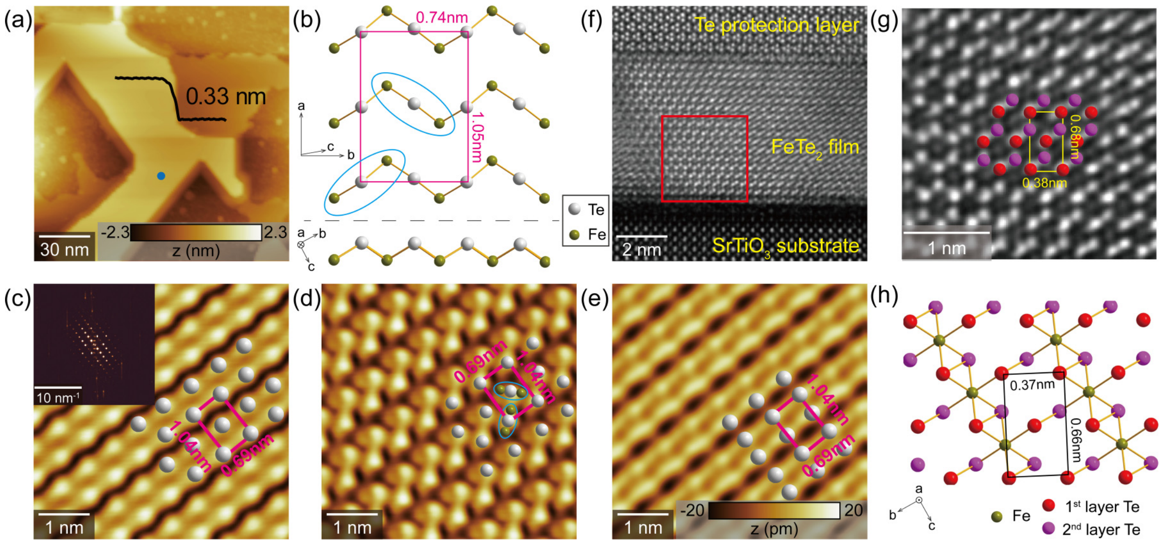

FIG. 3. The (011) surface of orthorhombic $FeTe_2$ films. (a) STM morphology of $FeTe_2$ films oriented along the [011] direction ($150 \times 150\,\mathrm{nm}^2$, $V_b = +2.0\,\mathrm{V}$, $I_t = 10\,\mathrm{pA}$). Inset is a line profile across the step edge of 0.33 ± 0.01 nm. (b) Top and side views of atomic structure for the (011) plane of $FeTe_2$ lattice, respectively. A rectangular 2×1 reconstruction of (0.74 ± 0.01) nm $\times$ (1.05 ± 0.01) nm is marked. The Te atoms bonding with neighboring Fe atoms are also marked as cyan ellipses. (c)–(e) The closeup STM images of the (011) surface at different bias voltages. The corresponding Fourier transformation of (a) is inserted in the top left corner. Toy models with 2×1 rectangle and lattice constants are superposed. In (d), the elongated Te atoms can be seen by cyan ellipses, corresponding to the bonding features of Te and Fe atoms in (b). Scanning conditions: $5 \times 5\,\mathrm{nm}^2$, $I_t = 50\,\mathrm{pA}$, $V_b = +120\,\mathrm{mV}$ for (c), -200 mV for (d), and $+1000$ mV for (e). (f) The cross-sectional STEM image of a typical $FeTe_2$ grown on $SrTiO_3$ substrate. The protective Te layer is also easy to resolve. (g) A zoomed-in ADF image from red square in (f). A toy model with unit cell and lattice constants is superposed. (h) Top view of atomic structure along the normal of (100) plane, reflecting the STEM results of cross section.

the cyan ellipses in Fig. 3(d). Such periodic features may be usually regarded as multiple-tip artifacts from STM images if the scanning tip is blunt, giving rise to several tunneling channels and false information on the atomic structure. We rule out this effect as follows: For the same STM region, such Te atoms simultaneously elongate toward different directions, and can only be visible at certain bias voltages. On the other hand, the nearest-neighbor Te-Te spacing along the *a* axis we observed (1.04 ± 0.01 nm) is twice the $FeTe_2$ lattice constant (0.53 nm), indicating a 2×1 surface reconstruction. At a scanning bias of +1.0 V, we visualize the missing Te atoms along the *a* axis in Fig. 3(e), where the centered Te atoms disappear, substantiating the 2×1 reconstruction. As the STM image is an expression of sample morphology convoluted with local DOS, our bias-dependent STM topographic images confirm the well-developed facet of the (011) plane from bulk $FeTe_2$.

To further confirm the structure of $FeTe_2$, we also carried out STEM experiments on the as-grown $FeTe_2$ films with Te protection layers, which are widely used for *ex situ* measurements identifying the atomic structures of epaxial materials [45]. Figure 3(f) displays an ADF image for $FeTe_2$ thin film along the [011] direction, where both the $SrTiO_3$ substrate and protective Te layers can be well resolved. Since the ADF intensity is closely related to the *Z* atomic number, Te atoms rather than Fe can be clearly seen as bright contrast in the zoom-in view of Fig. 3(g). Given that the ADF image is the cross section of the (011) plane, we can understand the observed pseudohoneycomb shape by the structural model in Fig. 3(h), which depicts the atomic arrangements along the normal that perpendicular to the (011) plane [Fig. 3(a)]. The elongated spots of the honeycomb are composed of two adjacent Te atoms with covalent bonds from the first and second layer, as shown by the red and pink balls, respectively. The measured lattice spacings from the horizontal and vertical direction are 0.38 ± 0.01 nm and 0.68 ± 0.01 nm, respectively, both reasonably agreeing with the corresponding lattice model. The consistency of STM and STEM analysis verifies the formation of $FeTe_2$ films via a low-temperature MBE growth.

Having unraveled the surface structure of $FeTe_2$ films in different orientations, we now turn to their electronic properties. Previously, no consensus has been reached on the band gap nature and magnetic structure of $FeTe_2$ compound after numerous studies. For instance, a GGA+*U* theoretical method declares that both marcasite and pyrite $FeTe_2$ are indirect semiconductors (0.27–0.34 eV) irrespective of their crystal structures [46,47], whereas Ghosh *et al.*, deliver a direct band semiconductor of calculated band gap as 0.88 eV [48]. A semiconducting gap of ~0.2 eV is reported with previous transport results on $FeTe_2$ single crystals [49], but much smaller than the value detected by the optical absorption spectrum of 0.67 eV [50]. To investigate the correlation between atomic geometry and electronic properties of our $FeTe_2$ films, we perform *in situ* low-temperature tunneling spectroscopy measurements on different surface terminations. Figure 4(a) displays a typical *dI/dV* spectrum taken on the (100) surface, possessing a semiconducting gap of ~185 meV. A sharp peak located at -78 mV is obviously seen near the valence band (VB) edge. On the basis of the first principles calculations, as shown in Fig. 4(b), we obtain an indirect band gap of 191 meV, qualitatively agreeing with the STS observations. It is clearly

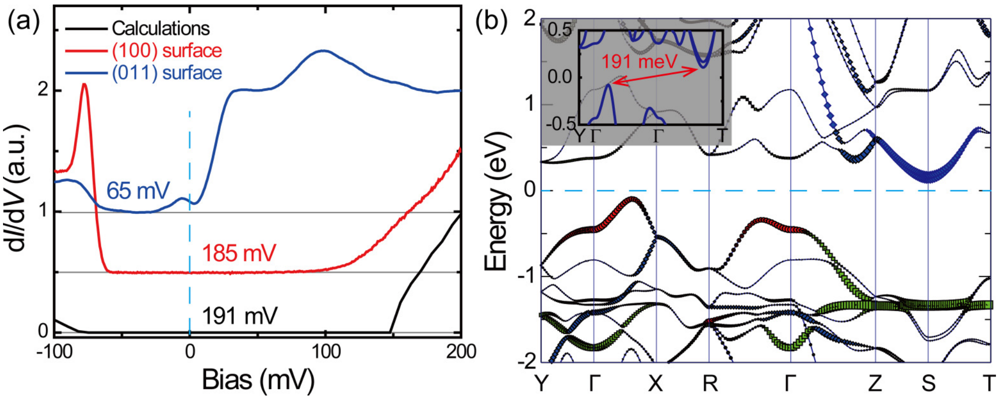

FIG. 4. Electronic structures of FeTe$_2$ films. (a) STS spectra recorded on the (100) and (011) terrace, showing a semiconducting gap of ∼185 and 65 meV, respectively, comparing to our theoretical calculations ($V_b = +0.2$ V, $I_t = 100$ pA, $V_{\mathrm{mod}} = +1.414$ mV$_{\mathrm{rms}}$). Each point spectrum is taken at the location of solid circle in Figs. 2(a) and 3(a) for the (100) and (011) surfaces, respectively. The energy range of calculated DOS is rescaled by shifting E_F to −80 meV for better comparison. All spectra are shifted along y axis for clarity. The gray horizontal lines represent the corresponding zero differential conductance for each curve. (b) Calculated band structure and orbital characters of bulk FeTe$_2$ by first-principles calculations. The band gap is indirect with the size of 191 meV, as amplified around the Fermi energy inset. The red, green, and blue symbols mark the contributions of p_z orbitals of Te, $d_z{}^2$ and d_{xz} orbitals of Fe, respectively. The size of the symbols corresponds to the weight of the states. The Fermi level is set as zero with dashed cyan lines.

seen that the states of the conduction band (CB) minimum are mainly constituted by the d_{xz} orbitals of Fe, and the VB maximum is comprised of the p_z orbitals of Te, but the $d_z{}^2$ orbitals of Fe are deeply buried inside the VB. Thus, the indirect band gap originates from the d_{xz} orbitals of Fe at the S point and the p_z orbitals of Te along the Γ-X direction. In stark contrast to the (100) facet, the STS on the (011) surface in Fig. 4(a) shows a small gap of ∼65 meV, with the CB edge sitting very close to the Fermi level. Recent magnetic measurements suggest that FeTe$_2$ will undergo a magnetic phase transition from antiferromagnetic to ferromagnetic order at 35 and 29 K for in plane and out of plane, respectively [50,51]. We thus speculate that the different electronic structure observed for the (100) and (011) planes may be related to the strong uniaxial magnetic anisotropy, as well as the observed 2 × 1 reconstruction on the (011) surface (Fig. 3).

Interestingly, the electronic structure is obviously modified near the crystalline boundaries for both (100) and (011) surfaces. As demonstrated in Figs. 5(b) and 5(e), the band gap evolves into a dip at the Fermi energy with a V-shaped background by approaching the step edge. To better resolve the reduced band gap size, we acquire a series of STS spectra along the magenta lines on the (100) and (011) terraces, respectively, in Figs. 5(a) and 5(d). As depicted from the step edge to the terrace in Figs. 5(c) and 5(f), states of enhanced conductance within the energy range of the bulk gap are clearly seen in the vicinity of the edge, with a spatial extension of ∼2–3 nm. Far away from the edge boundaries, the conductance of VB exhibits spatial distributions with clear periods, in line with the morphologies of the (100) and (011) surfaces, respectively. The CB branches show upwards band bending over a distance of ∼2 nm towards the edge, confirming the metallic edge states by charge depletion or accumulation at the metal-semiconductor interface. Considering that the electronic structure of FeTe$_2$ is extremely sensitive to its structural modulation [50], the metallic edge states and tunable band gap may be closely related to the possible FeTe$_6$ octahedron distortion, which should be different for the (100) and (011) planes, as well as the specific geometries of edge boundary. Further investigations are needed to clarify the issue of the

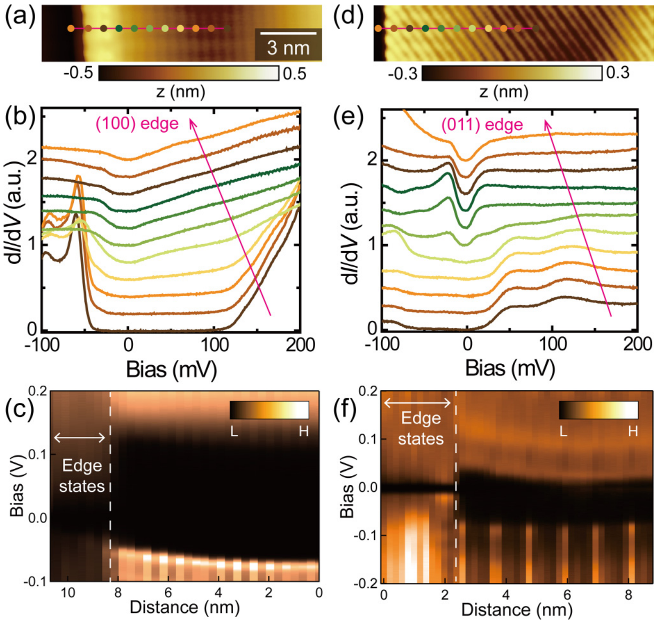

FIG. 5. Edge states of FeTe$_2$ films. (a) STM topography of the FeTe$_2$(100) surface containing a step edge (15×3 nm^2, $V_b = +0.1$ V, $I_t = 100$ pA). (b) Series of dI/dV spectra recorded near the step edge of the (100) terrace along the magenta line in (a), showing the gradual reduction of band gap size. The corresponding location of each point spectrum is indicated by the solid circle in (a) with the same color. The spectra are shifted along y axis for clarity. (c) 2D plot of tunneling spectra for (b) in spatial variation. The edge states are apparently seen when approaching the boundaries. Set points: $V_b = +0.2$ V, $I_t = 100$ pA, $V_{\mathrm{mod}} = +2.828$ mV$_{\mathrm{rms}}$. (d)–(f) The same as (a)–(c), but acquired near the FeTe$_2$(011) step edge.

local structural parameters and magnetic anisotropy in $FeTe_2$ thin films.

To summarize, we have epitaxially grown different stoichiometries of Fe-Te films via a temperature-controlled MBE method under high Te chemical potentials. STM and STEM are demonstrated to identify the structural and electronic characteristics for three phases of β-FeTe, α-FeTe, and $FeTe_2$, with the substrate temperature of ∼590, 550, and <470 K, respectively. The tunable band gap for different surfaces and the emergence of metallic states at the edge boundaries of $FeTe_2$ highly suggest the important role of structural distortion in determining its electronic and magnetic properties. Noting the recent growth of Fe-intercalated Fe_xTe_y films under Fe-rich conditions possessing a magnetic ground state [52], our work not only provides insight into the controllable synthesis of epitaxial Fe-Te compounds with variable stoichiometry, but also exhibits the versatility of engineering exotic electronic states for both Fe chalcogenides and transition metal dichalcogenides, including the single-layer $FeSe/SrTiO_3$ films.

This work was funded by the National Key Research and Development Program of China (Grants No. 2018YFA0307000, No. 2017YFA0403501, No. 2016YFA0401003, No. 2019YFA0308500), the National Science Foundation of China (Grants No. 11774105, No. 11874161, No. 11522431, No. 51991344), Beijing Natural Science Foundation (Grant No. Z190010), and the Strategic Priority Research Program of Chinese Academy of Sciences (Grant No. XDB07030200).

[1] F.-C. Hsu, J.-Y. Luo, K.-W. Yeh, T.-K. Chen, T.-W. Huang, P. M. Wu, Y.-C. Lee, Y.-L. Huang, Y.-Y. Chu, D.-C. Yan, and M.-K. Wu, Superconductivity in the PbO-type structure α-FeSe, Proc. Natl. Acad. Sci. USA **105**, 14262 (2008).

[2] E. Dagotto, Colloquium: The unexpected properties of alkali metal iron selenide superconductors, Rev. Mod. Phys. **85**, 849 (2013).

[3] Y. Mizuguchi and Y. Takano, Review of Fe chalcogenides as the simplest Fe-based superconductor, J. Phys. Soc. Jpn. **79**, 102001 (2010).

[4] Q.-M. Si, R. Yu, and E. Abrahams, High-temperature superconductivity in iron pnictides and chalcogenides, Nat. Rev. Mater. **1**, 16017 (2016).

[5] C.-L. Song, Y.-L. Wang, P. Cheng, Y.-P. Jiang, W. Li, T. Zhang, Z. Li, K. He, L.-L. Wang, J.-F. Jia, H.-H. Huang, C.-J. Wu, X.-C. Ma, X. Chen, and Q.-K. Xue, Direct observation of nodes and twofold symmetry in FeSe superconductor, Science **332**, 1410 (2011).

[6] K. Nakayama, Y. Miyata, G. N. Phan, T. Sato, Y. Tanabe, T. Urata, K. Tanigaki, and T. Takahashi, Reconstruction of Band Structure Induced by Electronic Nematicity in an FeSe Superconductor, Phys. Rev. Lett. **113**, 237001 (2014).

[7] A. Tamai, A. Y. Ganin, E. Rozbicki, J. Bacsa, W. Meevasana, P. D. C. King, M. Caffio, R. Schaub, S. Margadonna, K. Prassides, M. J. Rosseinsky, and F. Baumberger, Strong Electron Correlations in the Normal State of the Iron-Based $FeSe_{0.42}Te_{0.58}$ Superconductor Observed by Angle-Resolved Photoemission Spectroscopy, Phys. Rev. Lett. **104**, 097002 (2010).

[8] S. Medvedev, T. M. McQueen, I. A. Troyan, T. Palasyuk, M. I. Eremets, R. J. Cava, S. Naghavi, F. Casper, V. Ksenofontov, G. Wortmann, and C. Felser, Electronic and magnetic phase diagram of $\beta-Fe_{1.01}Se$ with superconductivity at 36.7 K under pressure, Nat. Mater. **8**, 630 (2009).

[9] B. Lei, J.-H. Cui, Z.-J. Xiang, C. Shang, N.-Z. Wang, G.-J. Ye, X.-G. Luo, T. Wu, Z. Sun, and X.-H. Chen, Evolution of High-Temperature Superconductivity From a Low-T_c Phase Tuned by Carrier Concentration in Fese Thin Flakes, Phys. Rev. Lett. **116**, 077002 (2016).

[10] M.-H. Fang, L. Spinu, B. Qian, H. M. Pham, T.-J. Liu, E. K. Vehstedt, Y. Liu, and Z.-Q. Mao, Superconductivity close to magnetic instability in $Fe(Se_{1-x}Te_x)_{0.82}$, Phys. Rev. B **78**, 224503 (2008).

[11] Q.-Y. Wang, Z. Li, W.-H. Zhang, Z.-C. Zhang, J.-S. Zhang, W. Li, H. Ding, Y.-B. OU, P. Deng, K. Chang, J. Wen, C.-L. Song, J.-F. Jia, S.-H. Ji, Y.-Y. Wang, L.-L. Wang, X. Chen, X.-C. Ma, and Q.-K. Xue, Interface-Induced High-temperature superconductivity in single unit-cell FeSe films on $SrTiO_3$, Chin. Phys. Lett. **29**, 037402 (2012).

[12] D. Liu, W. Zhang, D. Mou, J. He, Y.-B. Ou, Q.-Y. Wang, Z. Li, L. Wang, L. Zhao, S. He, Y. Peng, X. Liu, C. Chen, L. Yu, G. Liu, X. Dong, J. Zhang, C. Chen, Z. Xu, J. Hu, X. Chen, X.-C Ma, Q.-K. Xue, and X.-J. Zhou, Electronic origin of high-temperature superconductivity in single-layer FeSe Superconductor, Nat. Commun. **3**, 931 (2012).

[13] Q. Fan, W.-H. Zhang, X. Liu, Y.-J. Yan, M.-Q. Ren, R. Peng, H.-C. Xu, B.-P. Xie, J.-P. Hu, T. Zhang, and D.-L. Feng, Plain s-wave superconductivity in single-layer FeSe on $SrTiO_3$ probed by scanning tunnelling microscopy, Nat. Phys. **11**, 946 (2015).

[14] F. Arnold, J. Warmuth, M. Michiardi, J. Fikacek, M. Bianchi, Jin Hu, Z.-Q. Mao, J. Miwa, U. R. Singh, M. Bremholm, R. Wiesendanger, J. Honolka, T. Wehling, J. Wiebe, and P. Hofmann, Electronic structure of $Fe_{1.08}Te$ bulk crystals and epitaxial FeTe thin films on Bi_2Te_3, J. Phys.: Condens. Matter **30**, 065502 (2018).

[15] T. M. McQueen, Q. Huang, V. Ksenofontov, C. Felser, Q. Xu, H. Zandbergen, Y. S. Hor, J. Allred, A. J. Williams, D. Qu, J. Checkelsky, N. P. Ong, and R. J. Cava, Extreme sensitivity of superconductivity to stoichiometry in $Fe_{1+\delta}Se$, Phys. Rev. B **79**, 014522 (2009).

[16] Z.-N. Guo, F. Sun, B.-L. Han, K. Lin, L. Zhou, and W.-X. Yuan, Iron vacancy in tetragonal $Fe_{1-x}S$ crystals and its effect on the structure and superconductivity, Phys. Chem. Chem. Phys. **19**, 9000 (2017).

[17] H. Ru, Y.-S. Lin, Y.-C. Chen, Y. Feng, and Y.-H. Wang, Observation of two-level critical state in the superconducting FeTe thin films, Chin. Phys. Lett. **36**, 077402 (2019).

[18] Q. Li, W.-D. Si, and I. K. Dimitrov, Films of iron chalcogenide superconductors, Rep. Prog. Phys. **74**, 124510 (2011).

[19] D. Huang, T. A. Webb, C.-L. Song, C.-Z. Chang, J. S. Moodera, E. Kaxiras, and J. E. Hoffman, Dumbbell defects in FeSe Films:

A scanning tunneling microscopy and first-principles investigation, Nano Lett. **16**, 4224 (2016).

[20] W. Zhao, M. Li, C.-Z. Chang, J. Jiang, L. Wu, C. Liu, J. S. Moodera, Y. Zhu, and M.-H.-W. Chan, Direct imaging of electron transfer and its influence on superconducting pairing at FeSe/SrTiO$_3$ interface, Sci. Adv. **4**, eaao2682 (2018).

[21] W.-H. Zhang, Z. Li, F.-S. Li, H.-M. Zhang, J.-P. Peng, C.-J. Tang, Q.-Y. Wang, K. He, X. Chen, L.-L. Wang, X.-C. Ma, and Q.-K. Xue, Interface charge doping effects on superconductivity of single-unit-cell FeSe films on SrTiO$_3$ substrates, Phys. Rev. B **89**, 060506(R) (2014).

[22] Y. Hu, Y. Xu, Q.-Y. Wang, L. Zhao, S.-L. He, J.-W. Huang, C. Li, G.-D. Liu, and X. J. Zhou, Identification of a large amount of excess Fe in superconducting single-layer FeSe/SrTiO$_3$ films, Phys. Rev. B **97**, 224512 (2018).

[23] V. M. Pereira, C.-N. Wu, C.-E. Liu, S.-C. Liao, C.-F. Chang, C.-Y. Kuo, C. Koz, U. Schwarz, H.-J. Lin, C. T. Chen, L. H. Tjeng, and S. G. Altendorf, Molecular beam epitaxy preparation and in situ characterization of FeTe thin films, Phys. Rev. Materials **4**, 023405 (2020).

[24] C. Liu and K. Zou. Tuning stoichiometry and its impact on superconductivity of monolayer and multilayer FeSe on SrTiO$_3$, Phys. Rev. B **101**, 140502(R) (2020).

[25] W. Bao, Y. Qiu, Q. Huang, M. A. Green, P. Zajdel, M. R. Fitzsimmons, M. Zhernenkov, S. Chang, M. Fang, B. Qian, E. K. Vehstedt, J. H. Yang, H. M. Pham, L. Spinu, and Z.-Q. Mao, Tunable ($\delta\pi$, $\delta\pi$)-Type Antiferromagnetic Order in α-Fe(Te,Se) Superconductors, Phys. Rev. Lett. **102**, 247001 (2009).

[26] S.-L. Li, C. D. L. Cruz, Q. Huang, Y. Chen, J. W. Lynn, J.-P. Hu, Y.-L. Huang, F.-C. Hsu, K.-W. Yeh, M.-K. Wu, and P.-C. Dai, First-order magnetic and structural phase transitions in Fe$_{1+y}$Se$_x$Te$_{1-x}$, Phys. Rev. B **79**, 054503 (2009).

[27] C. Koz, S. Rößler, A. A. Tsirlin, S. Wirth, and U. Schwarz, Low-temperature phase diagram of Fe$_{1+y}$Te studied using X-ray diffraction, Phys. Rev. B **88**, 094509 (2013).

[28] A. Martinelli, A. Palenzona, M. Tropeano, C. Ferdeghini, M. Putti, M. R. Cimberle, T. D. Nguyen, M. Affronte, and C. Ritter, From antiferromagnetism to superconductivity in Fe$_{1+y}$Te$_{1-x}$Se$_x$ ($0 \leqslant x \leqslant 0.20$): Neutron powder diffraction analysis, Phys. Rev. B **81**, 094115 (2010).

[29] C. Trainer, C. M. Yim, C. Heil, F. Giustino, D. Croitori, V. Tsurkan, A. Loidl, E. E. Rodriguez, C. Stock, and P. Wahl, Manipulating surface magnetic order in iron telluride, Sci. Adv. **5**, eaav3478 (2019).

[30] Y. Song, X.-Y. Lu, L. P. Regnault, Y.-X. Su, H.-H. Lai, W.-J. Hu, Q.-M. Si, and P.-C. Dai, Spin-isotropic continuum of spin excitations in antiferromagnetically ordered Fe$_{1.07}$Te, Phys. Rev. B **97**, 024519 (2018).

[31] M. Enayat, Z. Sun, U. R. Singh, R. Aluru, S. Schmaus, A. Yaresko, Y. Liu, C. Lin, V. Tsurkan, A. Loid, J. Deisenhofer, and P. Wahl, Real-space imaging of the atomic-scale magnetic structure of Fe$_{1+y}$Te, Science **345**, 653 (2014).

[32] D. Fobes, I. A. Zaliznyak, Z. Xu, R. Zhong, G. Gu, J. M. Tranquada, L. Harriger, D. Singh, V. O. Garlea, M. Lumsden, and B. Winn, Ferro-Orbital Ordering Transition in Iron Telluride Fe$_{1+y}$Te, Phys. Rev. Lett. **112**, 187202 (2014).

[33] L. Kang, C. Ye, X. Zhao, X. Zhou, J. Hu, Q. Li, D. Liu, C. M. Das, J. Yang, D. Hu, J. Chen, X. Cao, Y. Zhang, M. Xu, J. Di, D. Tian, P. Song, G. Kutty, Q. Zeng, Q. Fu *et al.*, Phase-controllable growth of ultrathin 2D magnetic FeTe crystals, Nat. Commun. **11**, 3729 (2020).

[34] W. Li, W.-G. Yin, L.-L. Wang, K. He, X.-C. Ma, Q.-K. Xue, and X. Chen, Charge ordering in stoichiometric FeTe: Scanning tunneling microscopy and spectroscopy, Phys. Rev. B **93**, 041101(R) (2016).

[35] A. Mami, K. B. Messaoud, O. Kamoun, and M. Amlouk, Synthesis, physical study and efficient photocatalytic activity of FeTe$_2$, J. Mater. Sci.: Mater. Electron. **30**, 6050 (2019).

[36] K. B. Messaoud, J. Ouerfelli, K. Boubaker, and M. Amlouk, Structural properties of FeTe$_2$ thin films synthesized by tellurization of amorphous iron oxide thin films, Mater. Sci. Semicond. Process. **16**, 1912 (2013).

[37] H.-N. Xia, Y. Li, M. Cai, L. Qin, N.-L. Zou, L. Peng, W.-H. Duan, Y. Xu, W.-H. Zhang, and Y.-S. Fu, Dimensional crossover and topological phase transition in dirac semimetal Na$_3$Bi films, ACS Nano **13**, 9647 (2019).

[38] Q.-H. Zhang, X. He, J.-N. Shi, N.-P. Lu, H.-B. Li, Q. Yu, Z. Zhang, L.-Q. Chen, B. Morris, Q. Xu, P. Yu, L. Gu, K.-J. Jin, and C.-W. Nan, Atomic-resolution imaging of electrically induced oxygen vacancy migration and phase transformation in SrCoO$_{2.5-\sigma}$, Nat. Commun. **8**, 104 (2017).

[39] Y.-H. Yuan, W. Li, B. Liu, P. Deng, Z.-L. Xu, X. Chen, C.-L. Song, L.-L. Wang, K. He, G. Xu, X.-C. Ma, and Q.-K. Xue, Edge states at nematic domain walls in FeSe films, Nano. Lett. **18**, 7176 (2018).

[40] C.-L. Song, Y.-L. Wang, Y.-P. Jiang, Z. L, L.- L. Wang, K. He, X. Chen, X.-C. Ma, and Q.-K. Xue, Molecular-beam epitaxy and robust superconductivity of stoichiometric FeSe crystalline films on bilayer graphene, Phys. Rev. B **84**, 020503(R) (2011).

[41] D. S. Parker, Strong 3D and 1D magnetism in hexagonal Fe-chalcogenides FeS and FeSe vs. weak magnetism in hexagonal FeTe, Sci. Rep. **7**, 3388 (2017).

[42] Y. Kawashima, K. Ichimura, J. Ishioka, T. Kurosawa, M. Oda, K. Yamaya, and S. Tanda, Charge stripe structure in FeTe, Physica B (Amsterdam, Neth.) **407**, 1796 (2012).

[43] K.-F. Zhang, X.-L. Zhang, F. Yang, Y.-R. Song, X.-F. Chen, C.-H. Liu, D. Qian, W.-D. Luo, C.-L. Gao, and J.-F. Jia, Vectorial mapping of noncollinear antiferromagnetic structure of semiconducting FeSe surface with spin-polarized scanning tunneling microscopy, Appl. Phys. Lett. **108**, 061601 (2016).

[44] K. D. Oyler, X.-L. Ke, I. T. Sines, P. Schiffer, and R. E. Schaak, Chemical synthesis of two-dimensional iron chalcogenide nanosheets FeSe, FeTe, Fe(Se,Te), and FeTe$_2$, Chem. Mater. **21**, 3655 (2009).

[45] W.-H. Zhang, Y. Sun, J.-S. Zhang, F.-S. Li, M.-H. Guo, Y.-F. Zhao, H.-M. Zhang, J.-P. Peng, Y. Xing, H.-C. Wang, T. Fujita, A. Hirata, Z. Li, H. Ding, C.-J. Tang, M. Wang, Q.-Y. Wang, K. He, S.-H. Ji, X. Chen *et al.*, Direct observation of high-temperature superconductivity in one-unit-cell FeSe films, Chin. Phys. Lett. **31**, 017401 (2014).

[46] X.-H. Tian and J.-M. Zhang, The structural, elastic, electronic and optical properties of orthorhombic FeX$_2$, Superlattices Microstruct. **119**, 201 (2018).

[47] V. K. Gudelli, V. Kanchana, G. Vaitheeswaran, M. C. Valsakumar, and S. D. Mahanti, Thermoelectric properties of marcasite and pyrite FeX$_2$ (X = Se, Te): A first principle study, RSC Adv. **4**, 9424 (2014).

[48] A. Ghosh and R. Thangavel, Electronic structure and optical properties of iron based chalcogenide FeX$_2$ (X = S, Se, Te) for

photovoltaic applications: A first principle study, Indian J. Phys. **91**, 1339 (2017).

[49] H. Takashi, Transport properties of iron dichalcogenides $\mathrm{FeX_2}$ (X = S, Se and Te), J. Phys. Soc. Jpn. **67**, 1352 (1998).

[50] A. Rahman, D.-C. Zhang, M. U. Rehman, M. Zhang, X.-Q. Wang, R.-C. Dai, Z.-P. Wang, X.-P. Tao, and Z.-M. Zhang, Multiple magnetic phase transitions, electrical and optical properties of $\mathrm{FeTe_2}$ single crystals, J. Phys.: Condens. Matter **32**, 035808 (2020).

[51] J.-H. Zhang, W. Biao, C. J. O'Connor, and W. B. Simmons, Magnetic characterization of amorphous intermetallic materials $\mathrm{MTe_2}$ (M = Fe and Co), J. Appl. Phys. **73**, 5718 (1993).

[52] X.-X. Zhao, P. Song, C.-C. Wang, A. C. R. Jensen, W. Fu, Y. Deng, D.-Y. Wan, L.-X. Kang, S.-C. Ning, J.-D. Dan, T. Venkatesan, Z. Liu, W. Zhou, K. S. Thygesen, X. Luo, S. J. Pennycook, and K. P. Loh, Engineering covalently bonded 2D layered materials by self-intercalation, Nature (London) **581**, 171 (2020).